Smart Structures and Systems, *Vol. 12, No. 1 (2013) 023-039*
DOI:http://dx.doi.org/10.12989/sss.2013.12.1.023

Investigation of smart multifunctional optical sensor platform and its application in optical sensor networks

C. Pang[1], M. Yu[*1], A.K. Gupta[1] and K.M. Bryden[2]

[1]*Department of Mechanical Engineering, University of Maryland, College Park, USA*
[2]*Department of Mechanical Engineering, Iowa State University, Ames, USA*

(Received January 8, 2012, Revised August 29, 2012, Accepted November 20, 2012)

Abstract. In this article**,** a smart multifunctional optical system-on-a-chip (SOC) sensor platform is presented and its application for fiber Bragg grating (FBG) sensor interrogation in optical sensor networks is investigated. The smart SOC sensor platform consists of a superluminescent diode as a broadband source, a tunable microelectromechanical system (MEMS) based Fabry-Pérot filter, photodetectors, and an integrated microcontroller for data acquisition, processing, and communication. Integrated with a wireless sensor network (WSN) module in a compact package, a smart optical sensor node is developed. The smart multifunctional sensor platform has the capability of interrogating different types of optical fiber sensors, including Fabry-Pérot sensors and Bragg grating sensors. As a case study, the smart optical sensor platform is demonstrated to interrogate multiplexed FBG strain sensors. A time domain signal processing method is used to obtain the Bragg wavelength shift of two FBG strain sensors through sweeping the MEMS tunable Fabry-Pérot filter. A tuning range of 46 nm and a tuning speed of 10 Hz are achieved. The smart optical sensor platform will open doors to many applications that require high performance optical WSNs.

Keywords: microelectromechanical system; Fabry-Pérot tunable filter; wireless optical sensor network; multiplexing fiber Bragg grating; strain measurement

1. Introduction

Future smart systems (e.g., smart buildings, smart power plants, etc.) will require a large number of sensors that can provide detailed information on various ongoing processes within these systems. These sensors can be of the same type or different types located at different positions in the systems. A wireless sensor network (WSN) becomes an attractive option for addressing the requirements of these systems, which consists of spatially distributed sensor nodes to monitor physical or environmental conditions, acquiring information such as temperature, pressure, acceleration, vibration, and chemical species (Akyildiz 2002). To date, most conventional WSN nodes, particularly those used in commercialized products, rely on electrical or mechanical sensing principles (Crossbow Inc. 2007, Rice 2008, Vito 2011).

Compared with their counterparts, optical measurement methods have been proven to have the advantages of having immunity to electromagnetic interference (EMI), having large bandwidth and high sensitivity, being able to work in harsh environments, and being multiplexible. Among

∗Corresponding author, Associate Professor, E-mail: mmyu@umd.edu

http://www.techno-press.org/?journal=sss&subpage=8 ISSN: 1738-1584 (Print), 1738-1991 (Online)

various kinds of optical sensors, fiber Bragg grating (FBG) sensors are good candidates for distributed monitoring of various parameters due to their excellent multiplexibility. A FBG sensor consists of an optical fiber with a periodic perturbation of the refractive index at the core of the fiber. For a well-written FBG, the Bragg wavelength shifts with respect to various disturbances, such as strain and temperature. Since the FBGs were first developed, due to their excellent performance as sensor elements, FBGs have been used for both static and dynamic measurements. And their remarkable multiplexing capability renders them an attractive choice in high-density sensor networks.

To date, FBG sensors have been used in a variety of industrial applications, including structural health monitoring (Kerrouche 2009, Talebinejad 2009, Rodrigues 2011, Guo 2011), where WSNs recently received a lot of attention. In order to retrieve the information of Bragg wavelength shift from FBG sensors, different optical systems for Bragg grating demodulation have been studied. A conventional method of using a tunable laser along with an optical spectrum analyzer (OSA) to retrieve the Bragg wavelength location can hardly be used in a smart system due to the bulkiness, high cost, and complexity of this optical system. In another type of system, a diffraction grating is used to de-multiplex the optical signal from different FBGs into narrow wavelength bands that can be measured by using a photodetector array (Sano 2003, Chtcherbakov 2004). With this system, high-speed interrogation with a sweeping frequency of several kilohertz can be realized since optical signals in multiple wavelength bands can be acquired simultaneously. However, the wavelength tuning range is limited by the arrayed waveguide gratings (AWG), which requires that separations of the FBG wavelengths are much more than the bandwidths of the AWG channel to avoid cross talk. To cover a wavelength detection range of 32 nm, 40 channels will be needed for a channel spacing of 100 GHz. It is thus difficult to obtain a compact system due to the bulkiness of the photodetector array. Another system consisting of a superluminescent light-emitting diode (SLED), a tunable Fabry-Pérot filter, and a photodetector has also been explored. With this simple system as a basis, there have been a few attempts to develop compact, smart optical sensor devices for interrogating Bragg grating sensors (Lloyd 2007, Allan 2009). For example, devices with a sweeping speed of 0.1 nm/μs and a sweeping range of several tens of nanometers were achieved (Allan 2009). However, these devices were developed through integrating conventional optical components, which are large and bulky with relatively high power consumption (in the order of watts), making it difficult to integrate these devices into the sensor nodes of WSNs. Therefore, resources constrained optical WSNs that can accommodate high performance fiber optic sensors, such as FBG sensors, although much needed, still remain a challenge.

Recently, microelectromechanical systems (MEMS) technology has demonstrated its superior capability in miniaturizing and integrating complex systems, which has made it practical to scale down and integrate all the necessary optical components into a small footprint. In our recent work, a system-on-a-chip (SOC) optical sensor platform has been developed (Zhang 2009) and integrated with a conventional WSN module, rendering an optical sensor node that enables optical WSNs (Pang 2011). With the smart SOC sensor platform, high performance optical sensing with multiple Fabry-Pérot sensors has been demonstrated in a low coherence interferometric system configuration (Pang 2012). In this article, the untapped potential of the smart SOC multifunctional sensor platform is explored to study its capability of interrogating multiplexed FBG sensors, which is essential for achieving high-density optical sensor networks. The rest of the article is organized as follows. The principle of the smart multifunctional sensor platform is first presented, followed by a detailed discussion of its key component, a MEMS based tunable Fabry-Pérot filter. Further, experimental arrangement and experimental results of using this sensor platform for interrogation of two FBG strain sensors are discussed. Finally, the concluding remarks are provided.

2. Principle of the smart optical SOC multifunctional sensor platform

2.1 Overview of the smart multifunctional optical sensor platform

The schematic of the multifunctional sensor platform is illustrated in Fig. 1, which consists of an optical module and an electronic module. The optical module features a SOC optical system, consisting of a SLED chip as the light source, a MEMS tunable Fabry-Pérot filter for optical signal processing, and multiple photodetector chips for optical signal detection. Low coherence light from the SLED is first sent via a 1x2 optical fiber coupler to the tunable Fabry-Pérot filter. The reflected light from the Fabry-Pérot filter is then split and coupled via one or several couplers into multiple sensors such as Fabry-Pérot interferometer based sensors and FBG sensors, as shown in Fig.1. The transmitted (or reflected) light from each optical sensor is then coupled back to a photodetector. The number of channels and FBG sensors could be supported will be discussed in Sec. 4.

The electronic module includes a transimpedance amplifier (TA) to convert the photocurrent from the photodetector into voltage, a high-resolution 16-bit analog-to-digital converter (ADC) integrated with a digital filter for data acquisition and filtering, and a small onboard microcontroller (MCU). The MCU also utilizes an integrated digital-to-analog converter (DAC) to generate the tuning voltage for the MEMS filter.

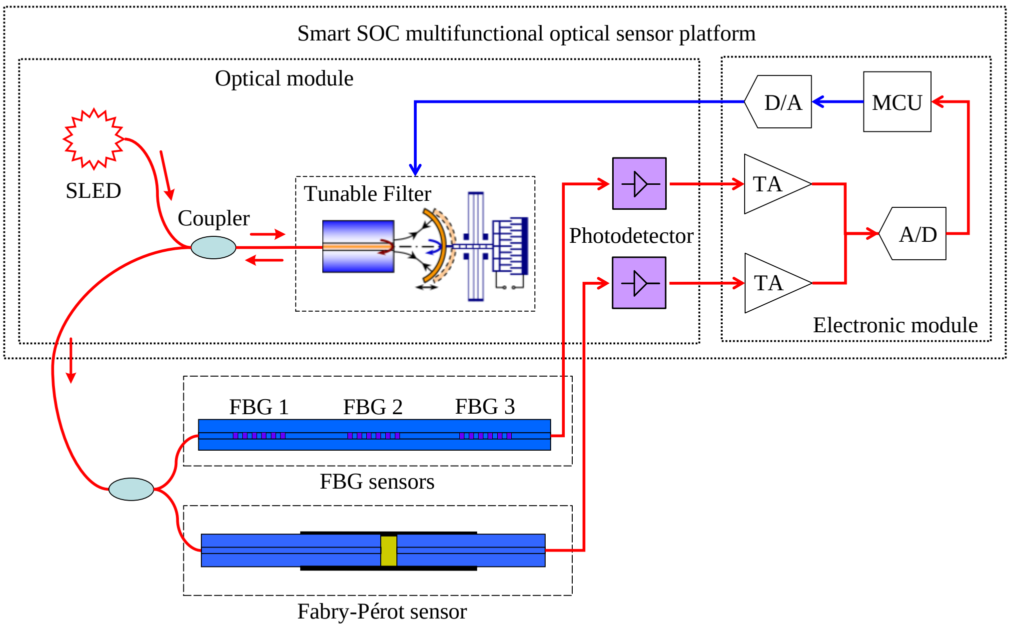

Fig. 1 Schematic of smart optical SOC sensor platform with different optical sensors

The optical module and the electronic module along with multiple optical sensors (e.g., Fabry-Pérot sensors or FBG sensors) form a multifunctional optical sensor platform, which can accommodate multiple heterogeneous optical sensors in different configurations for measuring various parameters such as strain, temperature, pressure, acoustic wave, and chemicals. These optical sensors can be mounted on board or used as sensor probes for remote sensing. Remote sensing capability of the system is useful for applications that require harsh environmental sensing, such as combustion engine monitoring and deep oil well sensing.

The optical module of the smart SOC sensor platform is developed by using hybrid integrations of several on-chip optical MEMS components and optical fiber waveguides. To develop the smart optical platform, a SLED chip (IPSDC1301, Inphenix Inc) is used as the broadband source, which emits the light with a center wavelength of 1325 nm and a power of 120 μW, and has a coherent length of 35 μm. InGaAs photodiode chips (DL-PD-300, DenseLight Semiconductor) with a responsivity of 0.9 A/W at 1300 nm are used as photodetectors. The most important component of the optical module is the MEMS tunable Fabry-Pérot filter, which will be discussed in Sec. 2.2.

Usually a thermoelectric cooler should be used to increase and stabilize the power output of the SLED. However, a thermoelectric cooler consumes too much electrical power; several hundreds of milliwatts power is needed to obtain a SLED output that is double the output without using the cooler. If the same amount of power had been supplied to the SLED, the optical output would be much larger even with the degradation due to heating. Therefore, it is not power-efficient to use the cooler in the optical WSNs, where the power resource is very limited. On the other hand, it is important to ensure the system performance in the absence of a cooler. It has been found in the experiment that variation of temperature only affects the power output of the SLED, but not its center wavelength. This means that the temperature change will have little impact to the normalization. However, in order to obtain a stable intensity for each sweep, every time when the SLED is initiated, a delay time (about 1 minute) should be set before the sweeping to allow the SLED to achieve the thermal equilibrium.

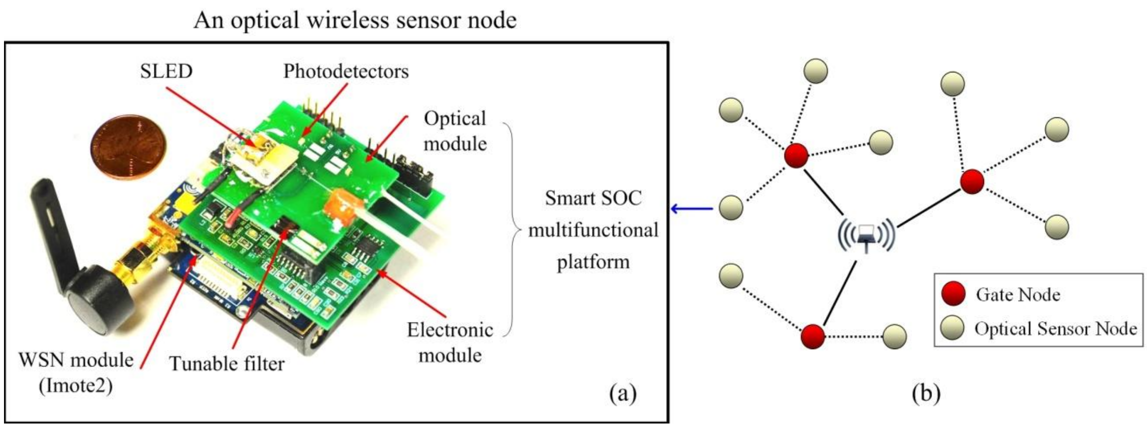

Fig. 2 (a) An optical wireless sensor node and (b) sample architecture of an optical WSN

To enable optical sensor networks, the smart SOC multifunctional sensor platform is integrated with a conventional WSN module (e.g., Imote2), rendering an optical WSN node, as shown in Fig. 2 (a).

The fully integrated optical WSN node has a dimension of 2.1" x 2.3" x 1.7". A sample architecture of optical WSNs is illustrated in Fig. 2 (b), in which each gate node is connected to a number of optical WSN nodes.

2.2 MEMS Fabry-Pérot tunable filter: fabrication, modeling, and characterization

The MEMS Fabry-Pérot tunable filter is the key optical component in the multifunctional optical platform. It is a Fabry-Pérot device constructed by using a micro-fabricated curved mirror and a well-cleaved single mode fiber (SMF28), shown in Fig. 3 (a). The curved mirror is attached to an electrostatic comb drive actuator to facilitate the tuning of the cavity length of the Fabry-Pérot filter. A scanning electron micrograph (SEM) of this MEMS filter is shown in Fig. 3 (b) and a close-up look of the Fabry-Pérot cavity is shown in Fig. 3 (c). The micromachined structures were fabricated by deep reactive ion etching (DRIE) using a silicon-on-insulator (SOI) wafer with a structural layer thickness of 25 μm. In order to expand the wavelength tuning range, the fiber end face was set to be as close to the curved mirror as possible, rendering an initial cavity length of 15 μm. Due to the DRIE process, the initial effective reflectivity of the curved mirror was rather low, which was measured to be approximately 4%, the same as that of a cleaved fiber. In order to get a much narrower full width at half maximum (FWHM) spectrum width as well as a higher finesse, a 100 nm silver layer was sputtered to the curved mirror and a 8 nm silver layer was sputtered to the cleaved fiber end face, resulting in a reflectivity of 90% for the curved mirror and 84% for the fiber end face. This greatly increased the finesse of the filter from 0.17 to 270.

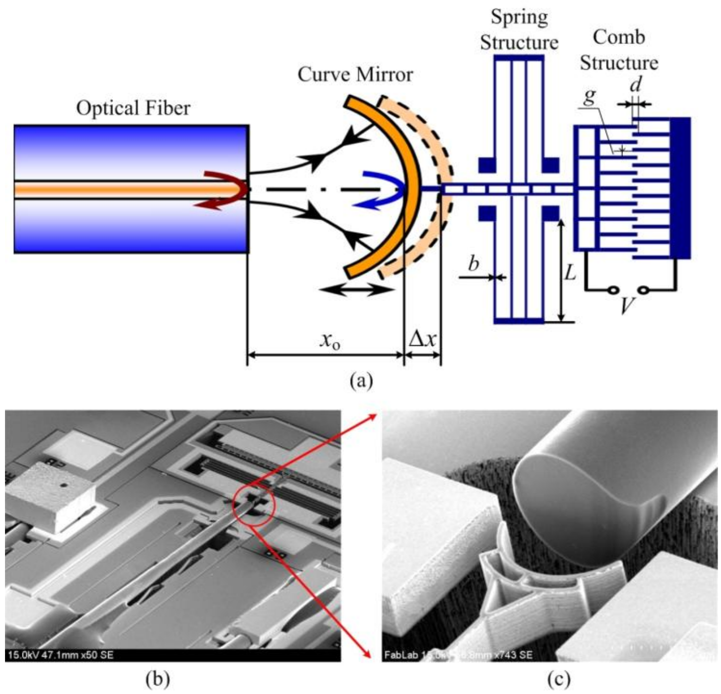

Fig. 3 (a) Schematic of the MEMS Fabry-Pérot tunable filter, (b) SEM of the MEMS tunable filter and (c) Close-up view of the Fabry-Pérot cavity

To understand the working principle of the MEMS filter, a mechanics model and an optics model of the MEMS Fabry-Pérot tunable filter are developed to study the relationship between the tuning wavelength and the applied voltage.

In the comb drive actuator, a movable set (rotor) and a stationary set (stator) of comb fingers are engaged. The capacitance between the stator and the rotor can be expressed as

$$C = \frac{2N\varepsilon_0 h(\Delta x + d)}{g} \tag{1}$$

where N is the number of fingers, ε_0 is the dielectric constant in air, h is the depth of the comb finger, d is the initial finger overlapping length when applied voltage is zero, Δx is the cavity length change, and g is the gap spacing between the fingers.

With an applied voltage of V, the electrostatic force produced by the comb drive actuator can be given by

$$F_s = \frac{1}{2}\frac{\partial C}{\partial(\Delta x)}V^2 = \frac{\varepsilon_0 Nh}{g}V^2 \tag{2}$$

The electrostatic comb drive is attached to a folded-flexure spring structure, as shown in Fig. 4 (a), in which the beams are anchored near the center and the trusses are not fixed to allow expansion or contraction of the beams along the x-axis. For a stiff truss, the structure model can be simplified as a clamped-clamped beam model (Tang 1993, Fedder 1994), as shown in Fig. 4 (b).

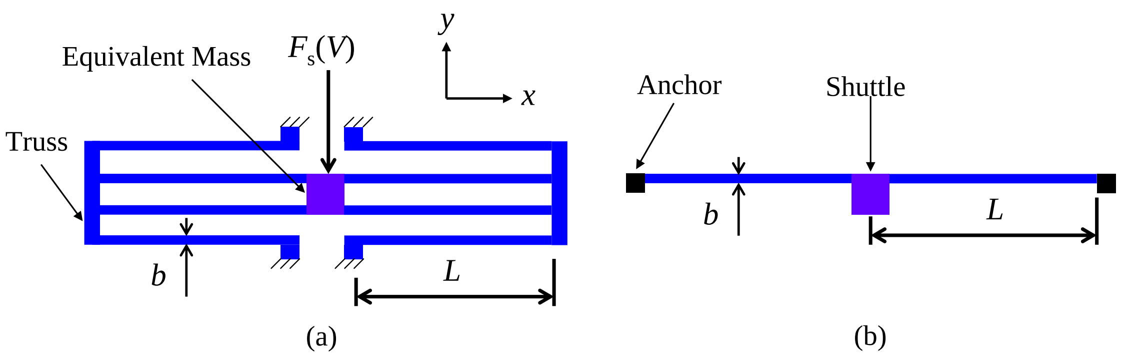

Fig. 4 (a) Folded-flexure spring structure attached to the comb drive actuator of the MEMS tunable filter and (b) simplified clamped-clamped beam model

The spring constant of the folded-flexure structure in y direction (the direction of the curved mirror movement) is

$$K_s = \frac{2Ehb^3}{L^3} \tag{3}$$

where E is the Young's modulus, b is the beam width, h is the beam depth (the same as the comb finger depth that from the same silicon layer of a SOI wafer in MEMS fabrication process), and L is the length of one beam segment.

The entire tunable Fabry-Pérot filter including the comb drive actuators can be modeled as a single degree-of-freedom vibration system. Because the fiber is bonded and fixed, when the curved mirror is driven at a frequency much below the natural frequency (2.57 kHz measured in the experiment) of the system, the cavity length x can be expressed as

$$x = x_0 + \frac{F_s}{K_s} = x_0 + \frac{\varepsilon_0 N L^3}{2gEb^3} V^2 \tag{4}$$

where x_0 is the initial cavity length of the Fabry-Pérot filter (~15 μm).

But the filter is not restricted to be only used in low frequency scenario, and more discussion of the filter sweeping frequency will be provided in Sec. 4.

Based on an optics model of the Fabry-Pérot interferometer, the transfer function of reflection H_r can be written as

$$H_r = \frac{F \sin^2(\frac{2\pi}{\lambda} x)}{1 + F \sin^2(\frac{2\pi}{\lambda} x)} \tag{5}$$

where $k_0 = 2\pi/\lambda$ is the free-space wave number, λ is the free-space wavelength, and F is the finesse that can be determined by the reflectivity of the two mirrors. Note that the reflection spectrum of the Fabry-Pérot interferometer reaches minimum at dip wavelengths λ_d when $\frac{2\pi}{\lambda_d} x = M\pi$, and thus, the dip wavelength can be written as

$$\lambda_d = \frac{2x}{M} = \lambda_0 + \frac{\varepsilon_0 N L^3}{gEb^3 M} V^2 \tag{6}$$

where λ_0 is the initial dip wavelength without any applied voltage and $\lambda_0 = \frac{2x_0}{M}$, and M is an integer.

Eq. (6) provides a theoretical prediction of the dip wavelength of the tunable Fabry-Pérot filter with respect to applied voltages. This relationship was also characterized in the experiment by using an OSA (86142B, Agilent, Inc) with an accuracy of ±0.01 nm. Based on Eq. (6), there can be many dip wavelengths within the spectrum width. The wavelength separation between adjacent reflection dips is referred as the free spectral range (FSR). In the experiment, the sweeping window was chosen when the voltage applied was increased from 0 to 5 V. Because the cavity length x is relatively small, the FSR is large enough to ensure that only one dip wavelength shows up in the sweeping window during each scan from 0 to 5 V. Without any voltage applied, the initial dip wavelength was measured to be 1292.4 nm. As the voltage increases, the cavity length keeps increasing. Because $\Delta x << x_0$, FSR is nearly unchanged and the single dip wavelength can be swept across the FSR, as shown in Fig. 5.

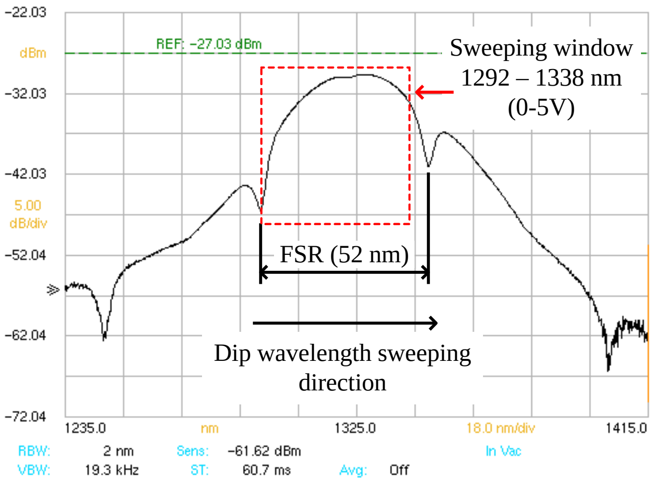

Fig. 5 Reflection spectrum of the MEMS Fabry-Pérot tunable filter obtained by using an OSA

Based on the Fabry-Pérot filter parameters listed in Table 1, of which the dimensional parameters were measured by using an optical profilometer (TMS 1200, Polytech) with an accuracy of 0.07%, the model predicted results are compared with those obtained from the experiments, as shown in Fig. 6. Thus, a calibration curve describes the dip wavelength as a function of the applied voltage square is obtained. As expected, the dip wavelength of the MEMS tunable Fabry-Pérot filter has a linear relationship with the applied voltage square, which is convenient for data processing.

Table 1 Parameters used for obtaining the simulation results

Parameter	Value
ε_0	8.85×10^{-12} F/m
N	120
L	540 μm
λ_0	1292.4 nm
E	169 GPa
b	2.5 μm
g	2.8 μm
h	25 μm

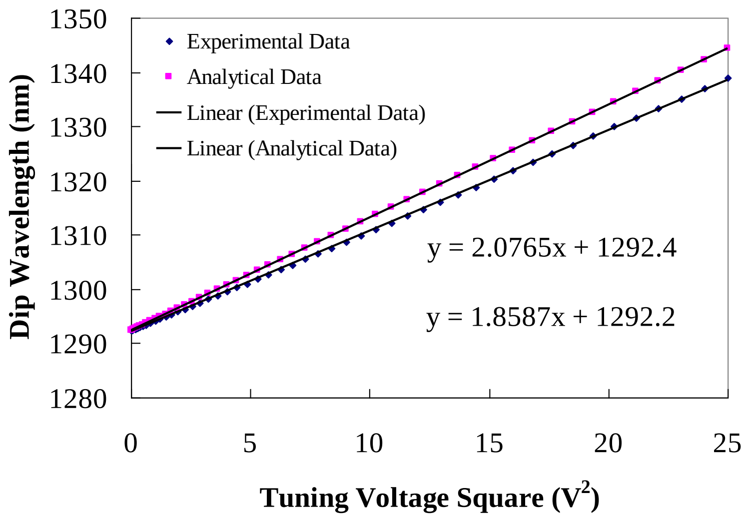

Fig. 6 Calibration of the MEMS tunable Fabry-Pérot filter for the dip wavelength tuning: comparison of the analytical and experimental results

The slope of the experimental data is slightly different from that of the analytical result. This discrepancy is believed to be due to the values of the beam width and the Young's modulus of silicon. Although the measurement of the beam width is accurate at the local measurement point, due to the fabrication resolution, the beam width inevitably varies along the beam length, which is 540 μm long. Since the slope is inversely proportional to the cubic of beam width, a slight variation in beam width measurement may incur a non-negligible difference in the slope. Furthermore, the Young's modulus of silicon is based on the value provided in the literature (Senturia 2001), which may differ from the actual value.

Compared to membrane actuated Fabry-Pérot filters (Irmer 2003), the comb drive actuated Fabry-Pérot filter requires a much smaller tuning voltage for achieving the same wavelength tuning range, which is much preferred in applications that require a low voltage and low power operation, such as in WSNs.

3. Smart multifunctional optical sensor platform for FBG sensor demodulation in optical WSNs

The smart multifunctional optical sensor platform can be used in a wide range of possible applications that require high performance optical sensing in a compact package. As mentioned previously, this platform can support many different types of optical sensors. For example, the platform can be used to enable a differential low coherence interferometer system to support various Fabry-Pérot sensors, which has been studied in our previous work (Pang 2011). In this paper, using this platform for interrogation of multiplexed FBG sensors is studied for the first time.

3.1 FBG demodulation scheme

For a system consisting of a SLED, a tunable Fabry-Pérot filter, and a photodetector, different FBG demodulation schemes have been studied. In one approach (Song 2000, Cusano 2004), the linear part of the Fabry-Pérot spectral response was utilized to obtain a high frequency measurement of FBG sensors, which greatly increased the measurement speed. However, the wavelength range that can be used was very limited and multiplexing cannot be realized. In another approach, a tunable Fabry-Pérot interferometer was used to sweep the optical signal in wavelength domain, but the signal was measured in time domain (Kersey 1993, Lioyd 2007, Allan 2009). This method requires only a single photodetector, and with a high finesse filter, it will allow for measuring multiplexed FBG sensors with a large wavelength range. In this work, the second approach is modified and implemented by using the smart SOC multifunctional optical sensor platform. In Fig. 7, the working principle of FBG sensor demodulation using the smart multifunctional sensor platform is illustrated.

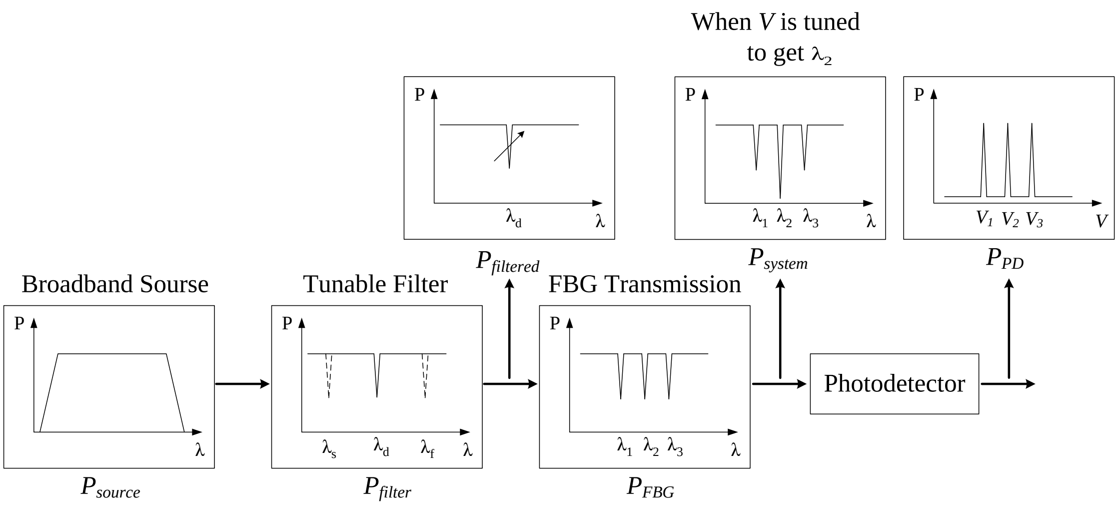

Fig. 7 Working principle of the smart SOC sensor platform for FBG sensor wavelength detection

$P_{source}(\lambda)$ represents the power spectrum of the SLED broadband source. When the light from the source is coupled into the MEMS tunable Fabry-Pérot filter, the reflected spectrum from the filter is illustrated as $P_{filter}(\lambda_d)$, where the dip wavelength λ_d depends on the applied voltage V. Depending on the bandwidth of the SLED and the working range of the tunable filer, the tunable wavelength range is from starting wavelength λ_s to finishing wavelength λ_f.

Before coupled to the FBG sensors, the spectrum of light reflected from the Fabry-Pérot filter is given as

$$P_{filtered}(\lambda) = P_{source}(\lambda) \cdot P_{filter}(\lambda_d) \tag{7}$$

which is an impulse function whose dip wavelength depends on the applied voltage. The light is then transmitted through the multiple FBG sensors with a transmission spectral response of

$P_{FBG}(\lambda_i)$, where λ_i represents each FBG sensor's Bragg wavelength. Note that the Bragg wavelength of each Bragg grating is designed to be within a different wavelength spectrum window, which defines the dynamic range of each Bragg grating sensor and facilitates wavelength division multiplexing. When registered at the photodetector, the output light spectrum of the overall optical system $P_{system}(\lambda)$ can be found as

$$P_{system}(\lambda) = P_{filtered}(\lambda) \cdot P_{FBG}(\lambda_i) \tag{8}$$

And the measured output power at the photodetector can be obtained as

$$P_{PD}(V) = \int P_{system}(\lambda) d\lambda \tag{9}$$

During the tuning process of the Fabry-Pérot filter, when the dip wavelength of filtered light overlaps with the Bragg wavelength of a FBG, a peak output power in $P_{PD}(V)$ can be detected and the voltage applied to the filter at this peak output power can be used to determine the dip wavelength of the filter (i.e., the Bragg wavelength of the FBG).

The entire signal processing process can be carried out by using the MCU and data acquisition components of the smart sensor platform, which is used to read the specified spectral response of the sensor and to incrementally adjust the applied voltage *V* for sweeping across the spectrum. The corresponding voltage *V* is then converted into the wavelength using the pre-calibrated relationship (see Fig. 6), and thus, the Bragg wavelength shift of FBG sensors can be retrieved.

3.2 Experiments and results

In the experiment, the smart sensor platform was combined with a wireless sensor networks module (Imote2, MEMSIC Inc.) to form an optical WSN node and an optical WSN was built, as shown in Fig. 8. To demonstrate this system's capability of interrogation of multiplexed FBG sensors, strain measurements with FBGs were carried out on an aluminum beam using a fiber containing two FBG sensors with Bragg wavelengths of 1302 nm and 1322 nm.

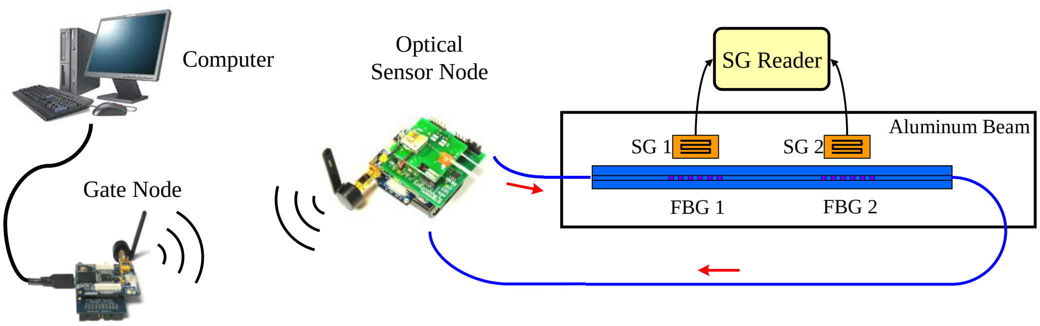

Fig. 8 Experimental setup for strain measurement using the optical sensor network with 2 FBG sensors. SG1 and SG2 are two strain gauges used as references

The fiber with two FBGs was mounted on an aluminum beam with a dimension of 300 mm x 25 mm x 2 mm. One end of the beam was clamped and the other end was loaded with a weight ranging from 0 to 540 g to introduce a tensile stress to the beam. Two strain gauges (SGD-1.5/120-LY11, Omega Inc) were also mounted near each FBG sensor and used as reference sensors.

A triangular wave with a voltage from 0 V to 5 V was generated by using the microcontroller to incrementally increase the voltage applied to the Fabry-Pérot filter, so that dip wavelength sweeping across its operating range can be achieved. At each step of the sweeping, the optical power was acquired and stored. The sweeping frequency was 10 Hz and the sampling rate for each scan was 2000 samples, rendering a sweep rate of 0.46 nm/ms and a sweep resolution of 0.023 nm. After each scan, the data was wirelessly transmitted back to the gate node connected to a computer. Based on the demodulation method described above, computer codes were developed to detect individual output signal peaks and convert them into the corresponding Bragg wavelength of each FBG.

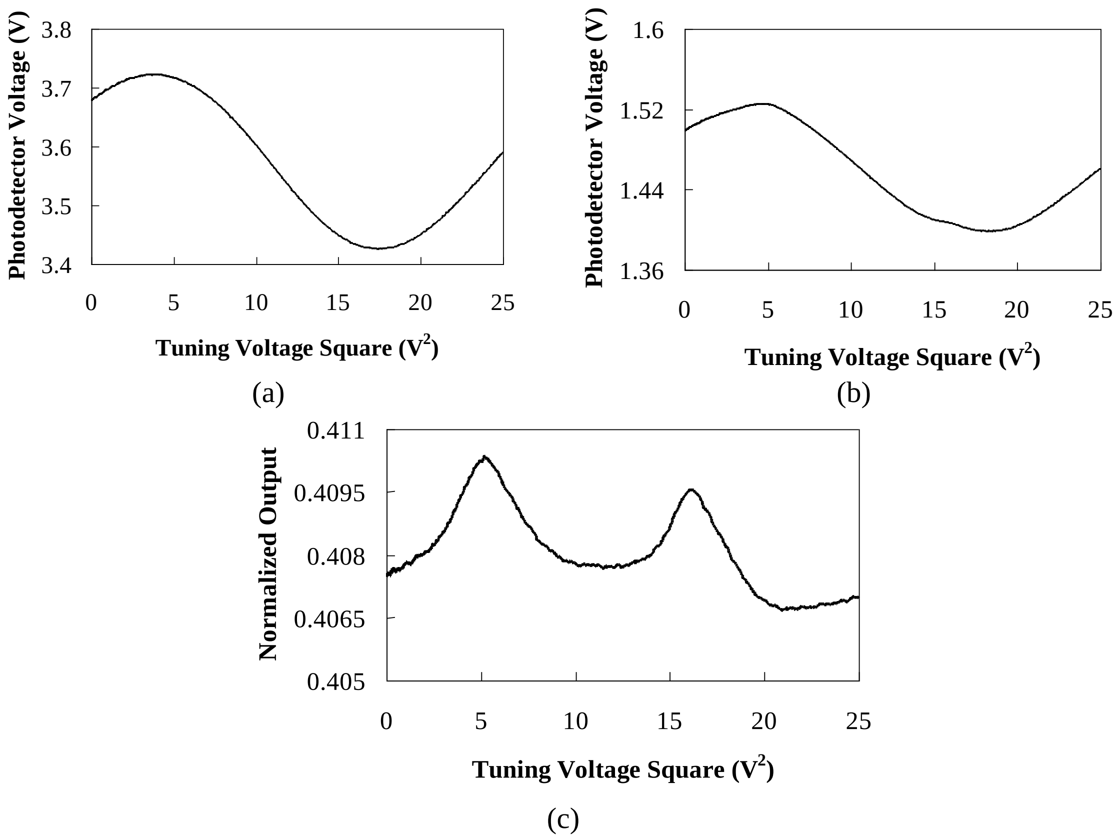

Fig. 9 Photodetector output as a function of tuning voltage square: (a) signal recorded without connecting FBG sensors, (b) signal recorded with FBG sensors before normalization, and (c) normalized signal

Because the SLED does not have a perfectly flat broadband, an additional step is needed to normalize the output power by the envelope of the SLED power spectrum. First, before connecting the FBGs with the optical sensor node, sweeping of the MEMS tunable Fabry-Pérot filter was carried out and the optical power output was recorded by using the photodetector as shown in Fig. 9 (a) (Data serial A). This step only needs to be done once before any real measurements and data obtained can be stored for future use. After connecting FBG sensors, another sweeping of the MEMS Fabry-Pérot filter was carried out and the optical power output as a function of V^2 was recorded, as shown in Fig. 9 (b) (Data serial B). To normalize the optical power, data serial B was divided by data serial A, which resulted in a data serial with much better peak visibility, allowing for easy peak detection, as shown in Fig. 9 (c).

Using the pre-calibrated curve of Fig. 6, the Bragg wavelength shifts of the two FBG sensors as a function of the applied strain can be obtained, as shown in Fig. 10. The applied strains were determined by using the strain gauges.

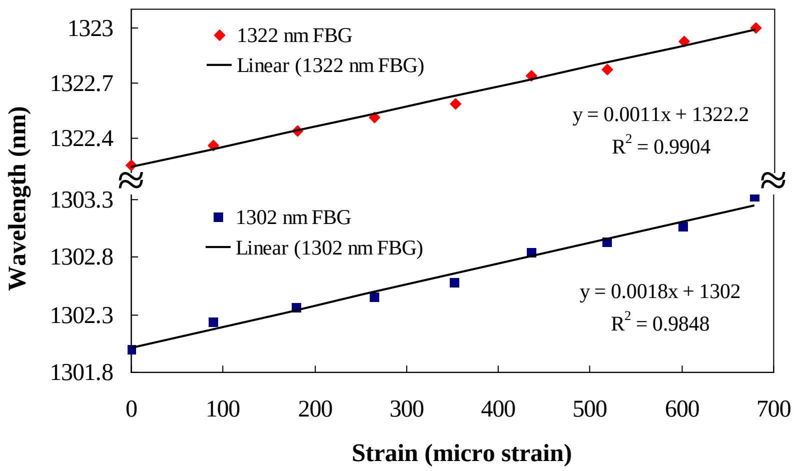

Fig. 10 Bragg wavelength shift versus strain obtained with two FBG sensors

As expected, a linear relationship can be observed in the results shown in Fig. 10. The two FBG sensors have different sensitivity is because they are from two different batches for different wavelength during fabrication. These results successfully demonstrate the capability of using the smart SOC optical sensor platform for demodulation of multiplexed FBG sensors in an optical WSN.

Since the measured strain is directly proportional to the peak wavelength shift, obtained by modulating the parameter V^2, it is easy to see that the strain resolution is determined by the resolution of the wavelength detection. As indicated in Eqs. (8) and (9), the amplitude of the output intensity peaks (shown in Fig. 9(c)) is mainly determined by the power of the SLED, the finesse of the filter, and the quality factor of the FBG sensors. With a large power output from the SLED and a high finesse filter, the obtained intensity peaks can be easily above the noise floor of the photodiode. For the photodiode used in the platform, the root mean square (RMS) noise level is 6 mV with circuit amplification. Under the current system arrangement with a 6 mV noise floor, the wavelength resolution is obtained to be 46 pm, which corresponds to a strain resolution of 25.6 με with the 1302-nm FBG. To further improve the strain resolution, a filter with a higher finesse can be used, which can be achieved by sputtering a thicker layer of gold to increase the reflectivity of the curved mirror and the fiber end face. For example, if the filter's FWHM is reduced to 20 pm (the same as that was used in the literature (Allen 2009)), a wavelength resolution of 4 pm will be achieved, rendering a strain resolution of 2 με with the same FBG.

Moreover, another factor to influence the strain resolution is the sweep resolution during each sweep, which is determined by the sampling frequency of the microcontroller. In this work, a sweep resolution of 23 pm is obtained at a sampling rate of 2 kHz in each sweep, which is smaller than the wavelength resolution determined by the photodiode noise floor. Therefore, the strain resolution of the system is still limited by the photodiode noise floor. However, if the sampling frequency is too low, the wavelength detection resolution may be limited by the sweep resolution rather than the photodiode noise floor, resulting in an even worse strain resolution.

According the discussion above, a high finesse (typically above 1000) Fabry-Pérot filter will help obtain a narrower and sharper dip wavelength for a better wavelength resolution. A higher finesse can be obtained by sputtering a thicker silver layer to the cleaved fiber end face to enhance the reflectivity. However, this will result in a lower optical power output because of the higher absorption of a thicker silver layer, which is another important aspect to be considered.

4. Discussions

4.1 Number of channels and sensors

The number of channels that the optical platform can support mostly depends on the output optical power of SLED. For the current system, it can support at least 2 channels, each with multiple FBGs serially arranged along a single fiber. If a cooler is used in the SLED or the input electrical power to the SLED is increased, the output power of SLED can be greatly enlarged to support more channels, but at the cost of increasing the power consumption.

For the number of multiplexed FBG sensors in one channel that can be supported by the platform, it depends on the tuning range and FWHM of the FP filter. To avoid cross talk, the maximum number of FBG sensors supported by the platform can be determined as the tuning range divided by the FWHM; that is, 46nm/5nm≈9 for this platform. If the finesse of the FP filter is increased (i.e., the FWHM of FP filter becomes smaller), more FBG sensors can be supported.

4.2 Sweeping frequency

Although only low frequency sweeping of the tunable FP filter has been demonstrated in this paper, it should be noted that the smart SOC optical sensor platform is not limited to the low frequency scenario. Theoretically, the system can be operated at a much higher frequency, even at the natural frequency. However, as the sweeping frequency is approaching the natural frequency, the dip wavelength will become a nonlinear function of V^2. In this case, determination of the dip wavelength based on the linear relationship will result in an error in the dip wavelength.

Since the mechanical structure of the FP tunable filter can be modeled as a single degree-of-freedom vibration system, the normalized amplitude frequency response of the structure is given by

$$\frac{\Delta x_f}{\Delta x} = \frac{1}{\sqrt{\left[1-(\frac{f}{f_0})^2\right]^2 + (2\varsigma\frac{f}{f_0})^2}} \tag{10}$$

where Δx_f is the FP cavity length change at a sweeping frequency of f, ζ is the damping factor (ζ was measured to be 0.02 in the experiment), and f_0 is the natural frequency. By using Eq.(10) along with Eq. (6), the error in the dip wavelength due to the increased sweeping frequency can be determined, which will increase as the sweeping frequency increases. For example, the error in the dip wavelength can be determined to be 0.03% at 10 Hz and 1.22% at 200 Hz. Since in the scope of this paper, the calibration result (see Fig. 6) was obtained at a static state, to reduce the error due to the increased sweeping frequency, only a low frequency scenario was demonstrated.

However, if a dynamic calibration of the dip wavelength can be carried out at a specific high sweeping frequency, by using the nonlinear calibration result, the error can be reduced considerably and the system can be operated at a much higher frequency.

Another way to operate the system at a higher frequency while still maintaining a good linearity, is to increase the stiffness of the spring structure to obtain a higher resonant frequency of the filter, so that the linear range can be extended. However, a larger voltage will be required to achieve the same wavelength tuning range.

4.3 Stability

Thermal issue is an important factor affecting the system's stability. For the SLED, as mentioned in Sec. 2.1, the normalization process will not be affected by temperature fluctuations, and the sweeping process will be carried out after the thermal equilibrium. The thermal characteristics of the MEMS tunable filter have been investigated in our previous work (Zhang 2009), where a linear change of cavity length with respect to temperature is observed. This temperature induced FP cavity length change can be compensated by using an on-site temperature sensor. Thus, an adjustment to Fig. 9(b) can be made, which will greatly reduce the temperature effect.

Vibrations and electrostatic forces can also affect the modulation characteristics of the comb structure. However, in our envisioned optical WSNs used in a harsh environment, the platform does not necessary to be positioned in the harsh environment, since it can be remotely connected with optical sensors that are survivable in the harsh environment by using optical fibers. Compared with traditional electrical/mechanical sensing systems that have on-board sensors or use metal wires to connect with sensors, optical fibers have immunity to electromagnetic interference and low attenuation loss over a long distance, making the optical sensor node capable of remote sensing in a harsh environment.

5. Conclusions

A smart SOC multifunctional optical sensor platform has been presented, which is capable of interrogating different kinds of optical sensors, including Fabry-Pérot sensors and FBG sensors. The key component of this platform, a tunable MEMS Fabry-Pérot filter, has been investigated to obtain better understanding of the working principle of the system. The platform has been combined with a WSN module to form an optical WSN, in which on-board data acquisition, processing, and wireless transmission can be achieved. The application of the smart multifunctional optical sensor platform in an optical WSN has been demonstrated for interrogating multiplexed FBG sensors. With this system, a large tuning range of 46 nm and a sweeping frequency of 10 Hz have been achieved. The smart multifunctional optical sensor platform along with the optical wireless sensor network node enabled by this platform is expected to significantly impact many fronts that require high performance optical sensors in high-density sensor networks.

Acknowledgements

Support received from US Department of Energy is gratefully acknowledged. The authors would like to thank Drs. Bob Romanasky, Susan Maley, and Steve Seachman for their help and support.

References

Akyildiz, I., Su, W., Sankarasubramaniam, Y. and Cayirci, E. (2002), "Wireless sensor networks: a survey", *Comput. Netw.*, **38**, 393-422.

Allan, W.R., Graham, Z.W., Zayas, J.R., Roach, D.P. and Horsley D.A (2009), "Multiplexed fiber Bragg grating interrogation system using a microelectromechanical Fabry-Perot tunable filter", *IEEE Sens. J.*, **9**(8), 936-943.

Chtcherbakov, A.A. and Swart. P.L. (2004), "Chirped fiber-optic Bragg grating interrogator in a multiplexed Bragg grating sensor configuration", *J. Lightwave Technol.*, **22**(6), 1543-1547.

Crossbow Technology, Inc. (2007), ITS400, Imote2 Basic Sensor Board, San Jose, CA.

Cusano, A., Cutolo, A., Nasser, J., Giordano, M. and Calabro, A. (2004), "Dynamic strain measurements by fibre Bragg grating sensor", *Sensor. Actuat. A-Phys.*, **110**(1-3), 276-281.

Fedder, G.K. (1994), *Simulation of microelectromechanical systems*, PhD Dissertation, Electrical Engineering and Computer Sciences, University of California, Berkeley, CA.

Guo, H., Xiao, G., Mrad, N. and Yao, J. (2011), "Fiber optic sensors for structural health monitoring of air platforms", *Sensors*, **11**(4), 3687-3705.

Irmer, S., Daleiden, J., Rangelov, V., Prott, C., Romer, F., Strassner, M., Tarraf, A. And Hillmer, H. (2003), "Ultralow biased widely continuously tunable Fabry-Perot filter", *IEEE Photonic. Tech. L.*, **15**(3), 434-436.

Kerrouche, A., Boyle, W.J.O., Sun, T. and Grattan, K.T.V (2009), "Design and in-the-field performance evaluation of compact FBG sensor system for structural health monitoring applications", *Sensor. Actuat. A-Phys.*, **151**(2), 107-112.

Kersey, A.D., Berkoff, T.A. and Morey, W.W. (1993), "Multiplexed fiber Bragg grating strain-sensor system with a fiber Fabry-Perot wavelength filter", *Optics Lett.*, **18**(16), 1370-1372.

Lloyd, S.W., Newman, J.A., Wilding D.R., Selfridge, R.H. and Schultz, S.M. (2007), "Compact optical fiber sensor smart node", *Rev. Sci. Instrum.*, **78**, 035108.

Pang, C., Yu, M., Zhang, X.M., Gupta A.K. and Bryden, K.M. (2011), "Multifunctional optical MEMS sensor platform for wireless optical sensor networks", *Proceedings of the 16th International Conference on Solid-State Sensors, Actuators and Microsystems (Transducers'11)*, Beijing, China, June.

Pang, C., Yu, M., Zhang, X.M., Gupta A.K. and Bryden, K.M. (2012), "Multifunctional optical MEMS sensor platform with heterogeneous fiber optic Fabry-Pérot sensors for wireless sensor networks", *Sensors and Actuators A-Physical*, http://dx.doi.org/10.1016/j.sna.2012.03.016.

Rice, J.A. and Spencer, B.F. (2008), "Structural health monitoring sensor development for the Imote2 platform", *Proceeding of the SPIE Smart Structures/NDE*, San Francisco.
Rodrigues, C., Felix, C. and Figueiras, J. (2011), "Fiber-optic-based displacement transducer to measure bridge deflections", *Struct. Health Monit.*, **10**(2), 147-156.
Sano, Y. and Yoshino, T. (2003), "Fast optical wavelength interrogator employing arrayed waveguide grating for distributed fiber Bragg grating sensors", *J. Lightwave Technol.*, **21**(1), 132-139.
Senturia, S.D. (2001), Microsystem Design, Springer.
Song, M., Yin, S. and Ruffin, P.B. (2000), "Fiber Bragg grating strain sensor demodulation with quadrature sampling of a Mach-Zehnder interferometer", *Appl. Optics*, **39**(7) 1106-1111.
Talebinejad, I., Fischer, C. and Ansari, F. (2009), "Serially multiplexed FBG accelerometer for structural health monitoring of bridges", *Smart Struct. Syst.*, **5**(4), 345-355.
Tang, W.C. (1990), *Electrostatic comb drive for resonant sensor and actuator applications*, PhD Thesis, Department of Electrical Engineering and Computer Sciences, University of California, Berkeley, CA.
Vito, S.D., Palma, P.D., Ambrosino, C., Massera, E., Burrasca, G., Miglietta, M.L. and Francia, G.D. (2011), "Wireless sensor networks for distributed chemical sensing: addressing power consumption limits with on-board intelligence", *IEEE Sens. J.*,**11**, 947-955.
Zhang, X.M., Liu, Y.X., Bae, H., Pang, C. and Yu, M. (2009), "Phase modulation with micromachined resonant mirrors for low-coherence fiber-tip pressure sensors", *Optics Express*, **17**, 23965-23974.